Evidence of kinetic-energy-driven antiferromagnetism in double perovskites: A first-principles study of La-doped Sr_2FeMoO_6

Prabuddha Sanyal, Hena Das, and T. Saha-Dasgupta
S.N. Bose National Centre for Basic Sciences, Kolkata 700098, India
(Received 8 July 2009; revised manuscript received 21 October 2009; published 11 December 2009)

Using first-principles density-functional calculations, together with exact diagonalization of Fe-Mo Hamiltonian constructed in a first-principles Wannier-function basis, we studied the electronic structure of La-doped double-perovskite compound Sr_2FeMoO_6. Our calculation shows stabilization of kinetic-energy-driven antiferromagnetic phase for La-rich compounds, in agreement with the results obtained on the basis of previous model calculations.

DOI: 10.1103/PhysRevB.80.224412 PACS number(s): 71.20.Be, 75.50.−y

I. INTRODUCTION

Double perovskites with a general formula $A_2BB'O_6$ where B and B' are transition-metal ions and A is a rare-earth or alkaline-earth ion, are materials that have attracted enormous amount of attention in recent time due to the diversity of their applications as, for example, in the field of spintronics [Sr_2FeMoO_6 (Ref. 1)], multiferroicity [Ba_2NiMnO_6 (Ref. 2)], magnetodielectric materials [La_2NiMnO_6 (Refs. 3 and 4)] and magneto-optic devices [Sr_2CrOsO_6 and Sr_2CrReO_6 (Ref. 5)]. The choice of B and B' ions, provide the tunability of B-O-B' interaction, giving rise to a variety of magnetic properties such as ferromagnetism, antiferromagnetism, ferrimagnetism, and electronic properties such as metallic, half metallic, and insulating.[6,7] The presence of two transition-metal ions instead of one as in perovskite material is expected to give rise to far more tunability and richness of properties compared to simple perovskites.

Perhaps the most studied member of this series that arose much interest is Sr_2FeMoO_6 (SFMO). This material was reported[1,8–12] to exhibit a large magnetoresistance(MR) effect with a fairly high ferromagnetic transition temperature of about 410 K, opening up the possibility of designing spintronics materials operating at room temperature. However, unlike colossal magnetoresistive compounds as manganites, this MR does not arise from electron-phonon interactions. Rather, it is extrinsic, of tunnelling magnetoresistive origin. Since the report of the large MR effect and high magnetic transition temperature, a number of experimental studies such as NMR,[13] x-ray emission spectroscopy,[14] Hall measurements,[15] and magnetic measurements[16] have been carried out to characterize various properties of this material. There have been also a number of theoretical studies involving both first-principles calculations[17–20] as well as model calculations.[21–26] The unusually high ferromagnetic transition temperature in Sr_2FeMoO_6 and related material such as Sr_2FeReO_6 was rationalized[17,23] in terms of a kinetic-energy-driven mechanism which produces a negative spin polarization at otherwise nonmagnetic site such as Mo or Re. Following this idea, a double-exchangelike two-sublattice model was introduced and studied by different groups.[21,22,24–26] While most of the studies[21,24,25] were restricted only to ferromagnetic phase, some of the studies[22,26] were extended to other competing magnetic phases too. Very recently,[27] the problem has been studied in detail in terms of a full numerical solution of spin-fermion model and as well as in terms of reduced, classical magnetic model. These studies predict that when the competing magnetic phases are taken into account, the electron-doped model systems beyond a certain doping prefers to have antiferromagnetic (AFM) arrangement of Fe spins compared to ferromagnetic (FM) arrangement of the undoped system. *The predicted antiferromagnetic phase in electron-doped system is kinetic-energy-driven rather than superexchange driven, as is the case, for example, in* Sr_2FeWO_6,[28] which is an insulating antiferromagnet with Néel temperature of ≈20 K. The superexchange-driven antiferromagnetic phase is necessarily insulating while the kinetic-energy-driven AFM phase may not be so. The prediction of such an antiferromagnetic phase of different origin is therefore of significance. While the kinetic-energy-driven antiferromagnetic phases have been suggested in hole-doped rare-earth manganites (e.g., the charge-exchange phase at half doping[29]), to the best of our knowledge, till date no reports of such analogous phases in double perovskites exist, thereby, opening up the possibility of experimental exploration in this front. However the aforementioned model calculations were carried out in two dimension and with single band, which was justified by the assumption that the dominant nearest-neighbor B-B' interactions are operative between orbitals of same symmetry and within a given plane. These restrictions are not strictly true. Furthermore, the magnetic ordering in real material is three dimensional. A full three-dimensional, all-orbital calculation without these approximations, is therefore necessary to put the possible existence of the AFM phase in firm footing.

Considering the above-mentioned points, it is therefore, of interest to study the problem of electron doping using first-principles density-functional theory (DFT) -based calculations. The first-principles calculations which take into account all the structural and chemical aspects correctly is expected to provide more realistic scenario and verification of predictions made by model calculations. The Sr ions in SFMO can be substituted for trivalent cations, such as La, leading to $Sr_{2-x}La_xFeMoO_6$. This would cause electron doping in the system, with $1+x$ electron per formula unit in the conduction band, compared to 1 electron per formula unit in the undoped SFMO situation. To our knowledge, there exists very few first-principles study of the La-doped SFMO sys-

tem. Few studies[30,31] that exist explored only the ferromagnetic phase, did not consider the other competing magnetic phases and were restricted mostly to Sr-rich part of the phase diagram. Motivated by the findings of the model calculations,[29] we considered it worthwhile to span the whole concentration range from $x=0.0$, i.e, Sr_2FeMoO_6 to $x=2.0$, i.e., La_2FeMoO_6 and study the relative stability of the various magnetic phases as one increases the carrier concentration through the increased doping of La.

We have carried out our study both in terms of full *ab initio* calculations as well as in terms of solutions of multiorbital, low-energy Hamiltonians defined in a first-principles-derived Wannier-function basis. The structural optimization and total-energy calculations of various magnetic phases have been carried out using the plane-wave pseudopotential method as implemented in the Vienna *ab initio* simulation package (VASP) (Ref. 32) while the doping effect in first-principles calculations has been simulated through supercell technique. The construction of low-energy Hamiltonian in first-principles-derived Wannier-function basis has been achieved through muffin-tin-orbital-based (MTO) based N-th order MTO(NMTO)-downfolding technique.[33] The constructed multiorbital, spin-fermion Hamiltonian defined in the first-principles-derived Wannier-function basis has been solved by means of real-space-based exact diagonalization technique.

The rest of the paper is organized in the following manner. Section II contains the details of the employed methods and calculations. Section III is devoted to results which consist of three subsections: (A) total-energy calculations, electronic structure, and relative stability of various magnetic phases in doped compounds, (B) determination of low-energy, few-orbital Hamiltonian by NMTO downfolding, and (C) calculations of magnetic phase diagram and magnetic transition temperatures in terms of low-energy Hamiltonian. The paper concludes with Sec. IV containing discussion and summary.

II. METHODS AND COMPUTATIONAL DETAILS

The first-principles DFT calculations were carried out using the plane-wave pseudopotential method implemented within VASP. We considered exchange-correlation functionals within generalized gradient approximation (GGA) (Ref. 34) and GGA+U.[35] We used projector-augmented wave potentials[36] and the wave functions were expanded in the plane-wave basis with a kinetic-energy cutoff of 450 eV. Reciprocal-space integration was carried out with a k-space mesh of $6\times6\times6$. Two sets of supercell calculations were carried out, one with two formula unit and another with eight formula unit. The two formula unit supercells with two inequivalent Fe atoms can accommodate the ferromagnetic spin alignment of Fe spins and the A-type antiferromagnetic spin alignments of Fe spins. The eight formula unit supercells with eight inequivalent Fe atoms in the unit cell, in addition to FM and A-type AFM, can accommodate G-type antiferromagnetic ordering of Fe spins (see Fig. 1)

For extraction of a few-band tight-binding Hamiltonian out of full DFT calculation which can be used as input to multiorbital, low-energy Hamiltonian-based calculations, we have carried out NMTO-downfolding calculations. Starting from a full DFT calculations, NMTO downfolding arrives at a few-orbital Hamiltonian by integrating out degrees which are not of interest. It does so by defining energy-selected, effective orbitals which serve as Wannier-type orbitals defining the few-orbital Hamiltonian in the *downfolded* representation. NMTO technique which is not yet available in its self-consistent form relies on the self-consistent potential parameters obtained out of linear muffin-tin orbital (LMTO) (Ref. 37) calculations. The results were cross checked among the plane wave and LMTO calculations in terms of total-energy differences, density of states (DOS), and band structures.

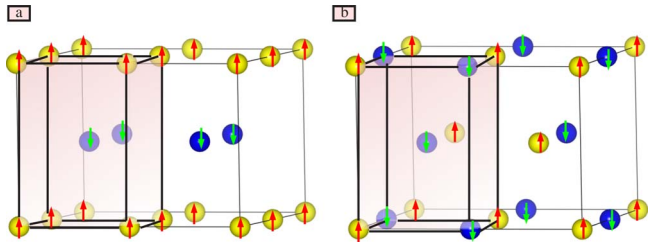

FIG. 1. (Color online) The Fe sublattice ordering of $Sr_{2-x}La_xFeMoO_6$. Shown are the A-type(left panel) and G-type (right panel) antiferromagnetic arrangement of Fe spins. In case of A-type antiferromagnetism the Fe spins in-plane are ferromagnetically coupled while Fe spins between two adjacent plans are antiferromagnetically coupled. For G-type antiferromagnetism, the Fe spins are antiferromagnetically coupled both out-of-plane and in-plane. The shaded box indicate the unit cell of two formula unit supercell.

The multiorbital, low-energy Hamiltonian that is assumed to capture the essential physics of SFMO, should consist of the following ingredients: (i) a large core spin at the Fe site, (ii) strong coupling on the Fe site between the core spin and the itinerant electron, strongly preferring *one* spin polarization of the itinerant electron, and (iii) delocalization of the itinerant electron on the Fe-Mo network.

From the above considerations, the representative Hamiltonian is given by

$$H = \epsilon_{\mathrm{Fe}} \sum_{i\in B} f^{\dagger}_{i\sigma\alpha} f_{i\sigma\alpha} + \epsilon_{\mathrm{Mo}} \sum_{i\in B'} m^{\dagger}_{i\sigma\alpha} m_{i\sigma\alpha} - t_{\mathrm{FM}} \sum_{\langle ij\rangle\sigma,\alpha} f^{\dagger}_{i\sigma,\alpha} m_{j\sigma,\alpha} - t_{\mathrm{MM}} \sum_{\langle ij\rangle\sigma,\alpha} m^{\dagger}_{i\sigma,\alpha} m_{j\sigma,\alpha} - t_{\mathrm{FF}} \sum_{\langle ij\rangle\sigma,\alpha} f^{\dagger}_{i\sigma,\alpha} f_{j\sigma,\alpha} + J \sum_{i\in A} \mathbf{S}_i \cdot f^{\dagger}_{i\alpha\mu} \vec{\sigma}_{\mu\nu} f_{i\alpha\nu}. \quad (1)$$

The f's refer to the Fe sites and the m's to the Mo sites. t_{FM}, t_{MM}, and t_{FF} represent the nearest-neighbor Fe-Mo, second-nearest-neighbor Mo-Mo, and Fe-Fe hoppings, respectively, the largest hopping being given by t_{FM}. σ is the spin index and α is the orbital index that spans the t_{2g} manifold. The difference between the t_{2g} levels of Fe and Mo, $\tilde{\Delta}=\epsilon_{\mathrm{Fe}}-\epsilon_{\mathrm{Mo}}$, defines the charge-transfer energy. Since among the crystal-field split d levels of Fe and Mo, only the relevant t_{2g} orbitals are retained, the on-site and hopping matrices are

TABLE I. Optimized cell parameters and the atomic positions for Sr_2FeMoO_6 and La_2FeMoO_6. Fe and Mo ions are situated at the high-symmetry Wykoff positions 2a and 2b, given by (0,0,0) and (0.0, 0.0, 0.5), respectively. For $I4/mmm$ symmetry Sr/La also sites in the high-symmetry Wykoff position given by (0.5, 0.0, 0.25) but sits in a general position for $P2_1/n$ symmetry.

	SFMO			LFMO							
	$I4/mmm$			$I4/mmm$				$P2_1/n$			
a		5.57		a		5.78		a		5.65	
b		5.57		b		5.78		b		5.63	
c		7.80		c		7.75		c		7.95	
								β		90.04	
	x	y	z		x	y	z		x	y	z
Sr	0.5	0.0	0.25	La	0.5	0.0	0.25	La	0.010	0.002	0.259
O1	0.248	0.248	0.0	O1	0.245	0.245	0.0	O1	0.504	0.000	0.255
O2	0.0	0.0	0.248	O2	0.0	0.0	0.245	O2	0.248	0.257	0.003
								O3	0.253	0.244	0.497

of dimension 3×3. The $\mathbf{S}_i$ are "classical" (large S) core spins at the B site, coupled to the itinerant B electrons through a coupling $J \gg t_{\mathrm{FM}}$.

Given the fact that $J \gg t_{\mathrm{FM}}$, the Hamiltonian of Eq. (1) can be cast into form appropriate for $J \to \infty$. This gives the following Hamiltonian, with "spinless" Fe conduction electrons and Mo electrons having both spin states,

$$H = t_{\mathrm{FM}} \sum_{\langle ij\rangle\alpha} \left[\sin\left(\frac{\theta_i}{2}\right) f^{\dagger}_{i\alpha} m_{j\uparrow\alpha} - e^{i\phi_i} \cos\left(\frac{\theta_i}{2}\right) f^{\dagger}_{i\alpha} m_{j\downarrow\alpha} \right] + \mathrm{H.c.}$$
$$+ t_{\mathrm{MM}} \sum_{\langle ij\rangle} m^{\dagger}_{i\sigma\alpha} m_{j\sigma\alpha} + t_{\mathrm{FF}} \sum_{\langle ij\rangle} \cos(\theta_{ij}/2)(f^{\dagger}_{i\alpha} f_{j\alpha})$$
$$+ \epsilon_{\mathrm{Fe}} \sum_i f^{\dagger}_{i\alpha} f_{i\alpha} + \epsilon_{\mathrm{Mo}} \sum_{i\sigma\alpha} m^{\dagger}_{i\sigma\alpha} m_{i\sigma\alpha}. \quad (2)$$

This is the lowest-energy Hamiltonian. There is no longer any "large" coupling in the Hamiltonian, and the number of degrees of freedom has been reduced to three per Fe site and six per Mo, compared to original problem with six degrees of freedom at both Fe and Mo sites. $m_{j\downarrow}$ and $m_{j\uparrow}$ hop to different conduction-electron projections at the neighboring Fe sites so the effective hopping picks up a θ_i, ϕ_i-dependent modulation. For example, $\theta=0$, $\phi=0$, corresponds to FM configuration with all Fe core spins being up. Since the spin S is large and can be considered classical, one can consider different spin configurations (ferro, antiferro, and disordered) and diagonalize the system in real space, to obtain variational estimates of the ground state, and its stability.

III. RESULTS

A. Total energy, electronic structure, and relative stability of magnetic phases

Sr_2FeMoO_6 crystallizes in body-centered tetragonal space group with $I4/mmm$ symmetry. The crystal structure of SFMO is well characterized. The crystal structure of La-doped Sr_2FeMoO_6 on the other hand is controversial. Some of the study[38,39] reports that though $I4/mmm$ symmetry is retained for small doping of La, for doping beyond $x=0.4$ or so, the symmetry changes to $P2_1/n$. The other measurements[30] however reports that all compounds of $Sr_{2-x}La_xFeMoO_6$ for $x=0$, 0.25, 0.5, and 1.0 crystallize in $I4/mmm$ symmetry. Unfortunately, the information of the detailed crystal structure data are limited due to the facts that (a) the compounds till now have been synthesized only for La concentrations less than or equal to 1, (b) increasing concentration of La leads to increased disorder which prohibits accurate measurement of the underlying symmetry. While in the following, we have primarily reported the results assuming $I4/mmm$ symmetry, we have also carried out calculation for $P2_1/n$ symmetry for the end member, La_2FeMoO_6 (LFMO). The crystal structure corresponding to $P2_1/n$ symmetry for La_2FeMoO_6 was obtained starting with initial parameters of $x=0.4$ as reported in Ref. 40 and then performing total-energy optimization of the initial structure. The $P2_1/n$ symmetry structure has been found to be energetically lower in energy by 90 meV than the corresponding $I4/mmm$-symmetry structure. However, as described later, the primary conclusion of our results is found to remain unaffected by this possible change in symmetry. Table I. shows the theoretically optimized crystal structures obtained using plane-wave basis,[41] of SFMO, and that of LFMO assuming $I4/mmm$ symmetry as well as $P2_1/n$ symmetry.

The volume for LFMO is found to expand with respect to that of SFMO, in agreement with experimental trend[30,38] of increasing volume with increased La doping. Assuming $I4/mmm$ symmetry, as is seen from Table I, the internal parameters corresponding to oxygen positions, which are the only free parameters within $I4/mmm$ space group, change little upon changing Sr by La. The unit-cell volume for various intermediate members of the series obtained by interpolation from the optimized lattice parameters of the end members using Vegar's law, 120.99 Å^3 for SFMO, 123.27 Å^3 for $Sr_{1.5}La_{0.5}FeMoO_6$, and 125.56 Å^3 for $SrLaFeMoO_6$, agree well with the experimental data available for $I4/mmm$ symmetry in terms of volume expansion, given by 121.4, 124.0, and 124.88 Å^3, respectively.[30] The crystal structure for the

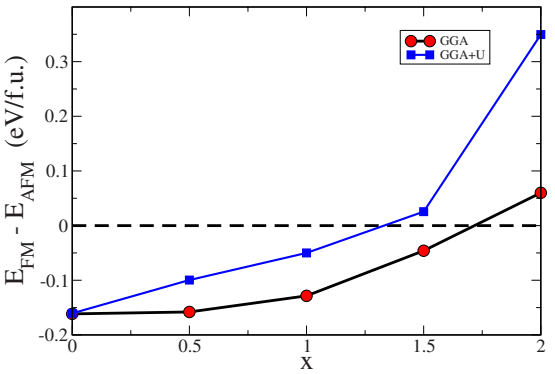

FIG. 2. (Color online) The energy difference between FM and AFM-*A* phase plotted as a function of La concentration. The FM phase becomes unstable beyond a critical concentration of La both within GGA and GGA+*U*.

doped compounds in the assumed $I4/mmm$ symmetry for the intermediate concentration values are, therefore, obtained by using Vegard's law for interpolation of cell parameters keeping the atomic positions fixed.

In the next step, we have carried out total-energy calculations of $Sr_{2-x}La_xFeMoO_6$ in $I4/mmm$ symmetry for the FM alignment of Fe spins and the AFM alignment of Fe spins, which for a two formula unit supercell is of *A* type (see Fig. 1). The energy difference between FM and AFM-*A* spin configuration per formula unit as a function of La concentration is plotted in Fig. 2. Calculations have been carried out both within GGA and GGA+*U*. Focusing on to GGA results first, as is evident from Fig. 2, the stability of the FM phase with respect to AFM configuration is gradually reduced as the La concentration is increased. As the concentration is increased beyond $x=1.5$ or so, the FM phase becomes unstable and the AFM phase becomes the ground state, in agreement with prediction of model calculations.[26,27] The total and magnetic moments at Fe and Mo sites, as obtained within GGA, are listed in Table II. The net magnetic moment at the FM phase reduces as the La concentration is increased, which is due to the increased moment at the Mo site. Such behavior has been also observed in experiment.[30] Especially, photoemission studies have confirmed that electron injection occurs at the Mo site, increasing the moment on that site.[42] While the moment at the Fe site stays more or less the same between

TABLE II. Magnetic moments at Fe and Mo sites, and the total magnetic moment in FM and AFM-*A* phase of $Sr_{2-x}La_xFeMoO_6$ in a two formula unit calculation. S3LFMO, SLFMO, and SL3FMO refer to $Sr_{1.5}La_{0.5}FeMoO_6$, $SrLaFeMoO_6$, and $Sr_{0.5}La_{1.5}FeMoO_6$, respectively.

		SFMO	S3LFMO	SLFMO	SL3FMO	LFMO
FM	Fe	3.68	3.59	3.53	3.50	3.52
	Mo	−0.23	−0.45	−0.71	−0.80	−0.85
	Total	4.0	3.5	3.0	2.5	2.0
AFM	Fe	3.69	3.60	3.52	3.42	3.50
	Mo	−0.05	−0.03	−0.04	−0.18	−0.70
	Total	0.0	0.0	0.0	0.0	0.0

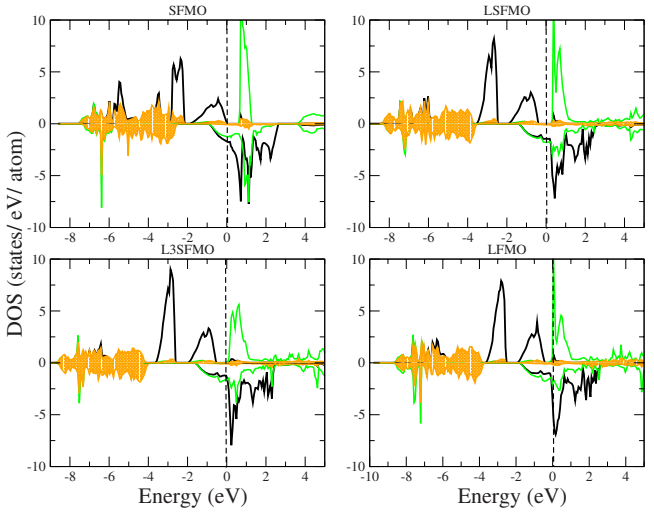

FIG. 3. (Color online) The GGA density of states corresponding to SFMO, SLFMO, $Sr_{0.5}La_{1.5}FeMoO_6$ (L3SFMO), and LFMO in ferromagnetic configuration. The density of states projected onto Fe, Mo, and O are represented by solid black, green (gray), and shaded gray area. The upper and lower panels correspond to majority- and minority-spin channels. Zero of the energy is set at the GGA Fermi energy.

ferromagnetic and antiferromagnetic phases, the magnetic moment at the Mo site is found to be systematically smaller in the AFM phase compared to FM phase.

In order to check the influence of the possible change in crystal symmetry that may happen between SFMO and LFMO, we have also calculated the total-energy difference between FM and AFM-*A* spin configurations, assuming LFMO in $P2_1/n$ symmetry with theoretically optimized structure. The calculated E_{FM}-$E_{AFM\text{-}A}$ came out to be 0.094 eV per formula unit, confirming the stabilization of AFM phase for LFMO. While the possible change in crystal symmetry from $I4/mmm$ to $P2_1/n$ for La-rich samples is expected to change the precise La concentration at which FM to AFM transition happens, the general trend of AFM phase becoming progressively more favorable upon increasing La doping therefore would remain hold good.

Figure 3 shows the GGA density of states corresponding to FM phase of SFMO, LFMO, and the doped compounds, $SrLaFeMoO_6$ and $Sr_{0.5}La_{1.5}FeMoO_6$ in $I4/mmm$ symmetry. Focusing on the well-studied[17] DOS of SFMO, we find that the Fe *d* states are nearly full (empty) in the majority (minority) -spin channel while the Mo *d* states are nearly empty in the majority-spin channel and partially filled in the minority-spin channel. This is in conformity with the half-metallic character of the compound and also with the nominal Fe^{3+} and Mo^{5+} valences. Due to the octahedral oxygen surrounding of Fe and Mo atoms, the Fe *d* and Mo *d* states are split up into t_{2g} and e_g, the highly delocalized state crossing the Fermi level in the minority-spin channel being of mixed Fe t_{2g}-Mo t_{2g} character. The empty Mo t_{2g} states in the majority-spin channel is found to be highly localized giving rise to peaked structure positioned at about 1 eV above the Fermi energy. As each of the Sr atoms is replaced by a La atom, one extra electron is introduced in the system

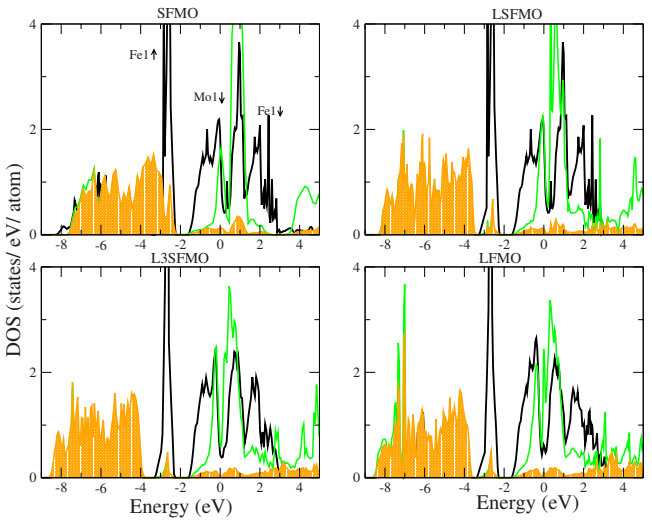

FIG. 4. (Color online) The density of states corresponding to SFMO, SLFMO, L3SFMO, and LFMO in the *A*-type antiferromagnetic configuration. The density of states projected onto Fe, Mo, and O are represented by solid black, green (gray), and shaded gray area. Zero of the energy is set at the GGA Fermi energy.

which populates the hybridized Fe t_{2g}-Mo t_{2g} state in the minority-spin channel, keeping the overall structure of the density of states intact. The Fermi level therefore progressively moves up like a rigid-band fashion as x is increased and eventually hits the Van Hove singularity of the Mo t_{2g} states in the majority-spin channel. The FM solution becomes unstable at this point. This is schematically shown in the left panel of Fig. 5. Interestingly the DOS corresponding to the mixed Fe t_{2g}-Mo t_{2g} character in the minority-spin channel also exhibits the singularity at the same energy due to the essentially two-dimensional-like nature of the hoppings between Mo t_{2g} and Fe t_{2g} Wannier functions as will be discussed in the following section.

Figure 4 shows the density of states of SFMO, LFMO, and the doped compounds, $SrLaFeMoO_6$ and $Sr_{0.5}La_{1.5}FeMoO_6$ in the antiferromagnetic *A* phase, as calculated within GGA. In the two formula unit supercells, there are two inequivalent Fe atoms, Fe1 and Fe2, whose spins are antiferromagnetically oriented. The majority channel of Fe1 therefore is identical to the minority channel of Fe2 and vice versa. The induced moments at two inequivalent Mo sites also become antiferromagnetically aligned, giving rise to a net AFM arrangement with a zero total moment. Shown in Fig. 4, are therefore, the partial DOS corresponding to one of the sublattice since that of the other sublattice is identical with majority and minority spins reversed. We find that the Mo-Fe hybridized state crossing the Fermi level, has a three peak Van Hove structure. This arises because of the fact that due to creation of sublattices in the AFM phase, the Mo hopping becomes restricted to a reduced dimension as the Mo electrons can effectively hop to Fe sites with a specific orientation of Fe spins and not in another. Interestingly, such a three-peak structure formation is also seen in model calculation (see Fig. 3 of Ref. 27). As found in the case of FM DOS, the gross features of the density of states remain unchanged with the La doping apart from the upward shift of

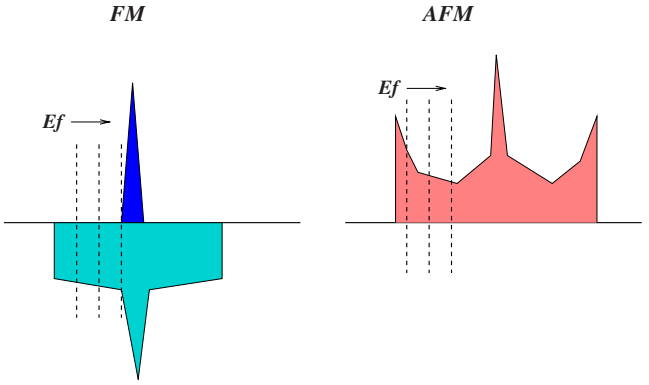

FIG. 5. (Color online) Schematic showing the mechanism stabilizing the AFM phase over FM phase. As the La doping is increased, the Fermi level (E_f) shifts toward right.

the Fermi energy. Reaching LFMO, the Fermi level lands up in the dip of the three-peak structured DOS, justifying the stability of the antiferromagnetic phase, as shown in the schematic of Fig. 5.

The antiferromagnetic state becomes energetically favorable, when the filling is such that it starts populating the Mo states in the majority-spin channel of the FM DOS, which is highly localized due to the strong preference of the Mo-Fe hopping in one spin channel and not in another. The antiferromagnetic configuration of Fe spins, on the other hand, allows both Mo down-spin as well as up-spin electron to hop, albeit in different sublattices, thereby stabilizing the AFM phase through kinetic-energy gain.

In order to check the influence of the missing correlation effect in GGA, we have also carried out GGA+U calculations with a typical U value[43] of 4 eV and J value of 1 eV, applied at the Fe site. The calculated energy difference between FM and AFM-*A* configuration as a function of La doping is shown in Fig. 2, along with GGA results. The application of U is found to increase the relative stability of AFM phase due to the increased superexchange contribution to antiferromagnetism in addition to kinetic-energy-driven antiferromagnetism.

In Fig. 6, we show the GGA+U DOS for LFMO, plotted for both FM and AFM-*A* phases. It is observed that the gross features of the DOS close to Fermi energy, remain similar to GGA, in particular, the Fermi energy in the FM phase remains pinned to the unoccupied Mo t_{2g} level in the FM phase. However, the hybridization between the Fe and Mo decreases. Nevertheless, the antiferromagnetic state is still found to have a finite density of states at Fermi energy, signifying the dominance of kinetic-energy-driven contribution over that of superexchange.

As already mentioned, considering the two formula unit supercell, the possible AFM arrangement that can be achieved is of *A* type. In order to achieve the *G*-type AFM ordering involving both in-plane and out-of-plane AFM ordering, one needs to increase the size of the supercell to at least eight formula unit. Eight formula unit supercells also allow to probe the concentration range intermediate to $x=1.5$ and $x=2.0$, the region where the crossover from FM to AFM happens. Since the qualitative conclusions remain un-

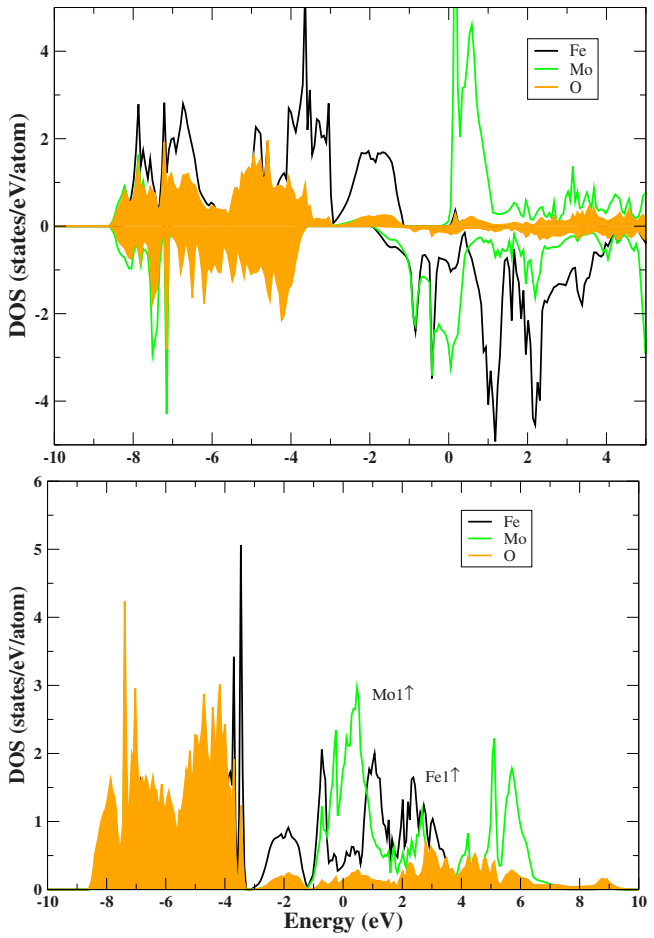

FIG. 6. (Color online) DOS for LFMO in FM and AFM-*A* phase, using GGA+*U*.

changed between GGA and GGA+*U*, the eight formula unit calculations were carried out only for GGA. The energy differences per formula unit obtained for different concentrations of La between FM and AFM-*A*, and between FM and AFM-*G* phases are listed in Table III. As found in the calculations with two formula unit, the stability of the FM phase is found to gradually decrease as the La concentration increases. Among the two antiferromagnetic phases, the *G*-type AFM is found to be energetically very close to *A*-type AFM

TABLE III. Total-energy differences per unit formula in eV between FM and AFM-*A*, and between FM and AFM-*G* for various doping of La, as obtained within eight formula unit supercell calculations.

	ΔE (FM-AFM-*A*)	ΔE (FM-AFM-*G*)
SFMO	−0.145	−0.147
SLFMO	−0.076	−0.073
$Sr_{0.5}La_{1.5}FeMoO_6$	−0.017	−0.008
$Sr_{0.375}La_{1.625}FeMoO_6$	0.014	0.006
$Sr_{0.25}La_{1.75}FeMoO_6$	0.037	0.032
$Sr_{0.125}La_{1.875}FeMoO_6$	0.057	0.052
LFMO	0.066	0.069

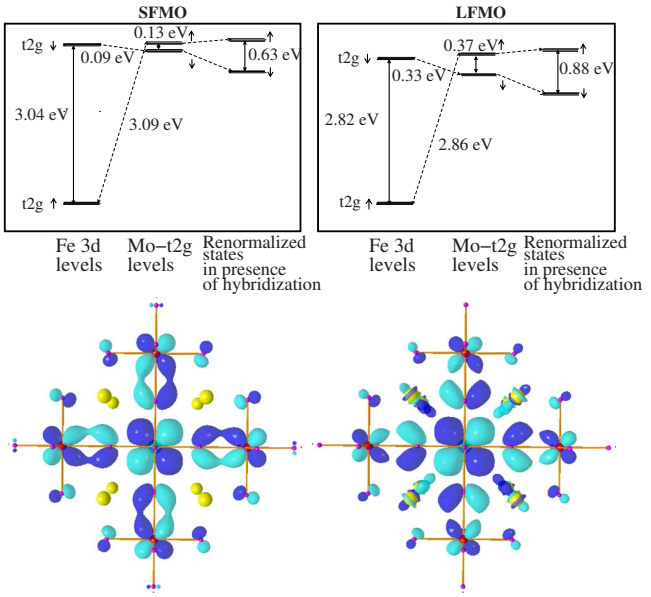

FIG. 7. (Color online) Top panels: Positioning of various energy levels as obtained by NMTO-*downfolding* calculation before and after switching on the hybridization between the magnetic and nonmagnetic ions. Bottom panels: Effective Mo t_{2g} Wannier orbitals corresponding to massively downfolded NMTO Hamiltonian in the down-spin channel. Shown are the orbital shapes (constant-amplitude surfaces) with lobes of opposite signs colored as blue (dark gray) and cyan (light gray). The central part of the Wannier orbitals are shaped according to Mo t_{2g} symmetry while the tails are shaped according to Fe t_{2g} and O-*p* symmetries. Significant amount of weights are seen in O and Fe site which reflects the strong hybridization between Fe, Mn, and O. For LFMO, finite weights are seen also at La sites, occupying the hollows formed between Mo-O and Fe-O bonds, which is of La $3z^2$ character.

phase, with *G*-type AFM being the ground state at the end limit of doping i.e., for LFMO.

B. Determination of low-energy, few-orbital Hamiltonian by NMTO downfolding

In order to probe the variation in La concentration in a continuous manner, it is perhaps more convenient to adopt a low-energy Hamiltonian approach. This would also allow one to calculate the physical properties such as magnetic transition temperatures, transport, and spin-wave spectra in a much more manageable way. For this purpose, however, it is essential to construct a realistic, low-energy Hamiltonian. We have used for this purpose, the NMTO-downfolding technique. For the present problem, we have derived a Fe t_{2g}-Mo t_{2g}-only Hamiltonian by integrating out all the degrees of freedom other than Fe t_{2g} and Mo t_{2g}. Calculations were carried out both in the spin-polarized and nonspin-polarized form. First of all, Fig. 7 illustrates the driving mechanism of magnetism in this class of compounds.[44] The top panels show the on-site energies of the real-space Hamiltonian defined in downfolded effective Fe-Mo basis for SFMO and LFMO in a spin-polarized calculation. As is seen, the t_{2g} levels of Mo appear in between the exchange-split Fe *d* states. Upon switching on the hybridization between

TABLE IV. Hopping matrix elements in eV between Fe t_{2g} and Mo t_{2g}. Only the hopping matrix elements of magnitude larger than 0.01 eV are listed. The on-site matrix elements are given by 0.005 (0.008), 0.0 (0.0), and 0.0 (0.0) eV for Fe-*xy*, Fe-*yz*, and Fe-*xz*, respectively, and 1.018 (1.057), 1.007 (1.053), and 1.007 (1.053) eV for Mo-*xy*, Mo-*yz*, and Mo-*xz*, respectively. All numbers inside the bracket are for LFMO and those outside are for SFMO. The energies for a given compound is measured with respect to the lowest-energy state. The small differences between numbers involving *xy* and that of *yz* and *xz* reflect the tetragonality present in the systems.

	Direction	*xy*, *xy*	*yz*, *yz*	*xz*, *xz*
1NN (Fe-Mo)	[100]	−0.26(−0.26)	−0.02(−0.04)	−0.26(−0.26)
	[010]	−0.26(−0.26)	−0.26(−0.26)	−0.02(−0.04)
	[001]	−0.02(−0.04)	−0.26(−0.25)	−0.26(−0.25)
2 NN (Fe-Fe)	[110]	−0.05(−0.06)	0.01(0.00)	0.01(0.00)
	[101]	0.00(0.00)	0.01(0.00)	−0.04(−0.06)
	[011]	0.00(0.00)	−0.04(−0.06)	0.01(0.00)
2 NN (Mo-Mo)	[110]	−0.11(−0.12)	0.00(0.01)	0.00(0.01)
	[101]	0.01(0.01)	0.00(0.01)	−0.11(−0.12)
	[011]	0.01(0.01)	−0.11(−0.12)	0.00(0.01)
3NN (Fe-Mo)	[111]	0.01(0.00)	0.00(0.00)	0.00(0.00)
4 NN (Fe-Fe)	[100]	0.01(0.01)	0.01(0.00)	0.01(0.01)
	[010]	0.01(0.01)	0.01(0.01)	0.01(0.00)
	[001]	0.01(0.00)	0.01(0.01)	0.01(0.01)
4 NN (Mo-Mo)	[100]	0.01(0.03)	0.01(0.00)	0.01(0.03)
	[010]	0.01(0.03)	0.01(0.03)	0.01(0.00)
	[001]	0.01(0.00)	0.01(0.03)	0.01(0.03)
5 NN (Fe-Mo)	[110]	−0.01(−0.01)	0.00(0.01)	0.00(0.00)
	[101]	0.00(0.01)	0.00(0.00)	−0.01(−0.01)
	[011]	0.00(0.00)	−0.01(−0.01)	0.00(0.01)

Fe *d* and Mo t_{2g}, states of same symmetry and spin interact. As a result, Mo t_{2g} up-spin states are pushed up in energy and Mo t_{2g} down-spin states are pushed down in energy, introducing a renormalized, negative spin splitting at the Mo site. The normalized spin splitting at Mo site is estimated by massive downfolding procedure by keeping only Mo t_{2g} states active in the basis, as shown in the right half on the top panels in Fig. 7. We note that this to be true for both SFMO and LFMO. This in turn, once again, reconfirms the hybridization driven mechanism to be operative both in SFMO and LFMO, the only difference being in the carrier concentration. This is in contrast to Sr2FeWO6 where W t_{2g} levels are pushed above the exchange split Fe *d* levels. The increase in the number of conduction electrons for LFMO compared to SFMO, is reflected in the spin splitting at Mo site before switching of the hybridization, to be about three times larger in LFMO (0.37 eV) compared to that of SFMO (0.13 eV). The bottom panels of Fig. 7 show the plots of Wannier functions of the massively downfolded Mo t_{2g} in the down-spin channel which demonstrates the hybridization between Mo t_{2g} and Fe t_{2g} states.

Table IV. shows the hopping interactions between Fe and Mo, obtained in the basis of Fe and Mo t_{2g} Wannier functions constructed by NMTO-downfolding technique. The numbers inside the bracket are that of LFMO while those outside are that of SFMO. The examination of the hopping table reveals that the nearest-neighbor Fe-Mo hopping to be strongest, as expected. The second-nearest-neighbor Mo-Mo hopping is half as strong as the nearest-neighbor Fe-Mo hopping while the second-nearest-neighbor Fe-Fe hopping is about one fifth of the nearest-neighbor Fe-Mo hopping. The out-of-plane hoppings which are of $dd\delta$ kind are order of magnitude smaller than the in-plane $dd\pi$ kind of hopping while interorbital hoppings are found to be negligibly small (less than 0.01 eV). This makes the hopping essentially two dimensional, as commented earlier. As is also evident, by replacing Sr by La, the essential material specific parameters of the low-energy Hamiltonian, as given in Eq. (1) changes very little. This is shown pictorially in Fig. 7, where it is found that the relative energy positions of the $t_{2g\downarrow}$ levels of Fe and Mo change very little in going from SFMO to LFMO. In the solution of low-energy Hamiltonians, to be described in the next section, calculations are therefore carried out assuming the hopping parameters corresponding to SFMO and varying the carrier concentration in a rigid-band fashion. The charge-transfer energy between Fe t_{2g} and Mo t_{2g} has been found to differ by about 5% which has been taken into account in these calculations.

C. Calculations of magnetic phase diagram and magnetic transition temperatures in terms of low-energy Hamiltonian

The exact diagonalization of the low-energy Hamiltonian, as given in Eq. (2) has been carried out for finite-size lattice

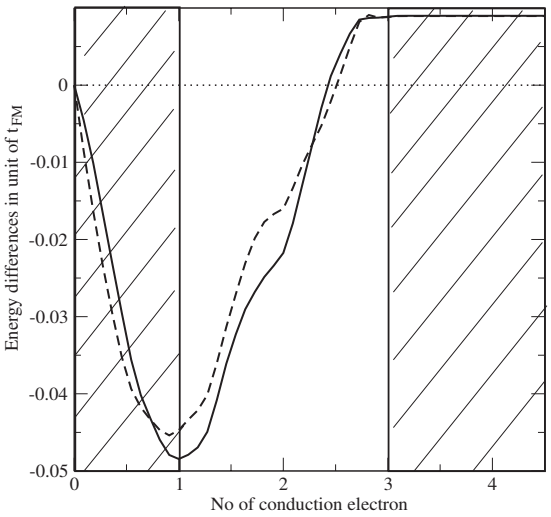

FIG. 8. The energy differences between the FM and *G*-type AFM phase (solid line) and the FM and *A*-type AFM phase (dashed line) plotted as a function of the number of conduction electrons, as obtained by exact diagonalization of the low-energy Hamiltonian for a $8\times8\times8$ lattice. Only the region outside the hashed regions, from carrier concentration 1 to 3 is of relevance for $Sr_{2-x}La_xFeMoO_6$.

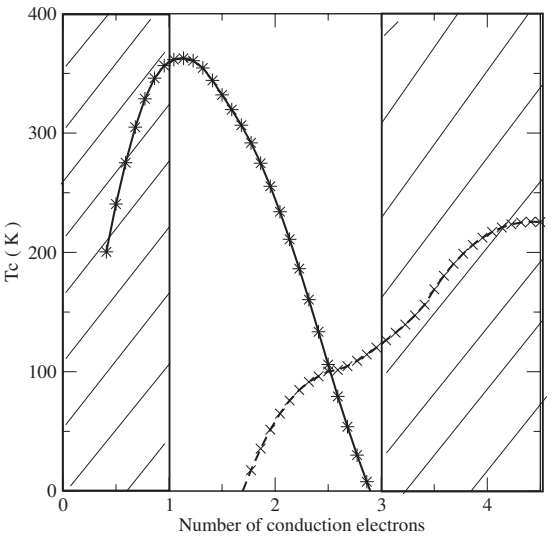

FIG. 9. The ferromagnetic T_c (solid line) and the antiferromagnetic transition temperature T_N (dashed line) plotted as a function of the number of conduction electrons, as obtained by exact diagonalization of the low-energy Hamiltonian for a $8\times8\times8$ lattice. As in Fig. 8, the region outside the hashed regions, from carrier concentration 1 to 3 is of relevance for $Sr_{2-x}La_xFeMoO_6$.

of dimensions $4\times4\times4$, $6\times6\times6$, and $8\times8\times8$. The hopping parameters and the on-site energies were taken out of DFT calculations, as listed in Table IV. For convenience of calculation, we have neglected the small tetragonality reflected in the parameters listed in Table IV. The dominant hopping interaction which is between nearest-neighbor Fe and Mo is found to be on the order of 0.3 eV while the spin-exchange splitting at Fe site as shown in Fig. 7, is on order of the 3 eV, an order of magnitude larger than the dominant hopping interaction. This justifies the assumption of $J\rightarrow\infty$ limit as adopted in Eq. (2). This makes the rank of the Hamiltonian to be diagonalized as $9/2\times N^3$ for a $N\times N\times N$ lattice.[45]

The energy difference between ferromagnetic configuration and *G*-type and *A*-type antiferromagnetic configuration of Fe spins as a function of carrier concentration is plotted in Fig. 8. The negative values of the energy differences indicate the stability of the ferromagnetic phase while the positive values indicate the stability of the antiferromagnetic phase. The crossover happens for a value of conduction electrons equal to about ~2.6, corresponding to $x=1.6$, which agrees well with the results of eight formula unit supercell calculations, given the assumption of infinite Hund's coupling at Fe site and the finite-size effect. This agreement is nontrivial since the effective Hamiltoanian has only 12 spin orbitals, and hence 12 bands, as compared to the 500 band calculation with eight formula unit supercells. This in turn, validates the construction of low-energy model Hamiltonian as given in Eq. (2), in terms of correct identification of the essential contributing terms. This gives us confidence in the constructed low-energy model Hamiltonian, which can henceforth be used to calculate many other properties such as conductivity, susceptibility, magnetoresistance, including at finite temperature, which are not easily accessible within DFT.

As an example, we have used the solutions of the low-energy Hamiltonian to calculate the magnetic transition temperatures by calculating the difference between the paramagnetic phase and the relevant magnetic phases. The paramagnetic phase was simulated as disordered local-moment calculations, where the calculations were carried out for several (~50) disordered configurations of Fe spin and were averaged to get the energy corresponding to paramagnetic phase. We note that, such a calculation would have been rendered extremely difficult within *ab initio* owing to the computational time involved using large supercells, and also averaging them over myriad configurations. Figure 9 shows the transition temperatures plotted as a function of carrier concentration. The ferromagnetic transition temperature at carrier concentration of 1, which corresponds to SFMO compound, is found to be 360 K in comparison to measured value of 410 K.[19] The ferromagnetic T_c is found to decrease upon increasing La concentration, and finally becomes zero. Upon suppression of ferromagnetic T_c, the transition temperature of the antiferromagnetic phase, T_N starts growing, hitting a maximum value for the end member, LFMO.

IV. SUMMARY AND OUTLOOK

Using the combination of first-principles DFT calculations and exact diagonalization calculations of low-energy Hamiltonians, we showed that the La-doped Sr_2FeMoO_6 compounds become progressively more unstable toward ferromagnetism as the La concentration is increased. For the La-rich members of $Sr_{2-x}La_xFeMoO_6$ series with $x>1.6$, the ground state becomes antiferromagnetic. This antiferromagnetic phase is found to be governed by the kinetic-energy-driven mechanism as operative in SFMO and achieved by

change in carrier concentration. In contrast to the superexchange-driven antiferromagnetic phase found in case of double perovskite such as Sr_2FeWO_6,[28] this antiferromagnetic phase presumably is metallic. Our DFT calculations found antiferromagnetic solutions with finite density of states at Fermi energy. The preliminary calculations of the matrix elements of the current operator also turned out to be nonzero. This will be taken up with more rigor in near future.

It is interesting to compare our results with dynamical mean-field theory (DMFT) calculations done by Chattopadhyay and Millis,[21] using a one-band model Hamiltonian. This was, however, a single-site calculation, and hence there was no possibility of capturing an antiferromagnetic phase. Their T_c vs N plot for the ferromagnetic phase, however, was very similar to ours, as shown in Fig. 9, in the sense that the T_c first increased, and then decreased with increasing filling, finally, becoming 0 at a filling close to 3. The additional and the most important finding of our study is that our calculations also demonstrate the cause of the vanishing T_c, namely, the emergence of the AFM phase.

There are however, several important issues which needs to be considered. Formation of pure La_2FeMoO_6 to best of our knowledge is not been reported in literature, which presumably is due to relative scarcity of Mo^{3+} ions in octahedral environment. La-rich SFMO samples, therefore seem more promising candidates for exploration of the antiferromagnetic phases.

Another important issue to bother about is the issue of antisite disorder, which has not been considered in our study. The necessary conditions of formation of double perovskites with ordered, rock-salt arrangement of B and B' transition-metal ions are that the size difference between B and B' ions should be sufficiently large as well the nominal charge difference. With the increase in La concentration, the extra doping electrons populate the Mo t_{2g} down-spin subband crossing the Fermi energy. As a result, the Mo^{+5} nominal valence in SFMO becomes Mo^{+5-m} in the doped compounds, m being the number of doped electron with a maximum value of 2. This decreases the charge difference between Fe^{+3} and Mo. This is expected to be detrimental to the ordering, though the ionic radii difference between Fe^{3+} (0.645 Å) and Mo^{3+} (0.69 Å) is larger than that between Fe^{3+} and Mo^{5+} (0.65 Å). The study on SFMO in this context,[46] find that even for a disordered sample, as given by x-ray study, the local ordering is maintained with a domain structure. Annealing conditions can give rise to domain structures with varying sizes of the domain. This gives us the hope in the observation of the antiferromagnetic phase in the La-rich SFMO samples. Attempts are already being made to prepare these overdoped samples locally, and preliminary results suggest existence of magnetic phases different from ferromagnetic phase.[47] On theoretical front, effect of disorder has been studied by Alonso *et al.*[26] Within a variational mean-field framework, they found that the filling/doping at which the T_c goes to zero increases upon increasing antisite disorder. This means that antisite disorder stabilizes the ferromagnetic phase. In other words, the antisite disorder is expected to reduce the stability of the antiferromagnetic phase, which is also seen in our preliminary calculations. We wish to carry out systematic study of the antisite disorder in future, keeping in mind possible formation of domain structures.

Finally, within the kinetic-energy-driven mechanism, the ferromagnetism gets destabilized and the antiferromagnetism wins when the carrier concentration reaches such a value that the B' d states gets filled up in one spin channel and tries to populate the other spin channel. Such situation is encountered also in case of another double perovskite, Sr_2CrOsO_6. Os being in nominal 5+ state, is in d^3 configuration with completely full Os t_{2g} states in the down-spin channel and lies within exchange-split energy levels of Cr t_{2g},[48] a case very similar to La_2FeMoO_6. Sr_2CrOsO_6, in contrast to above expectation, however stabilizes in ferromagnetic configuration of Cr spins. In this context, we found that the delicate balance between FM and AFM, is governed by the extent of hybridization between the localized B site and delocalized B' site. For Sr_2CrOsO_6, due to the movement of the Os t_{2g} within the exchange-split energy window of Cr t_{2g} in comparison to that of Mo t_{2g} within the exchange-split energy window of Fe d, the hybridization effect is weakened and also the finite spin-orbit coupling at Os site mixes the up- and down-spin channels, causing possibly the energy gain due to antiferromagnetism to be reduced.[48]

We believe our study will stimulate further experimental activities to explore the possibilities of double perovskites exhibiting kinetic-energy-driven antiferromagnetism.

ACKNOWLEDGMENTS

The authors gratefully acknowledge discussions with D. D. Sarma, P. Majumdar, M. Azuma, and J. Gopalakrishnan. T.S.D. acknowledges the support of Advanced Materials Research Unit and Swarnajaynti grant.

[1] K.-I. Kobayashi, T. Kimura, H. Sawada, K. Terakura, and Y. Tokura, Nature (London) **395**, 677 (1998).
[2] M. Azuma, K. Takata, T. Saito, S. Ishiwata, Y. Shimakawa, and M. Takano, J. Am. Chem. Soc. **127**, 8889 (2005).
[3] N. S. Rogado, J. Li, A. W. Sleight, and M. A. Subramanian, Adv. Mater. (Weinheim, Ger.) **17**, 2225 (2005).
[4] H. Das, U. V. Waghmare, T. Saha-Dasgupta, and D. D. Sarma, Phys. Rev. Lett. **100**, 186402 (2008).
[5] H. Das, M. De Raychaudhury, and T. Saha-Dasgupta, Appl. Phys. Lett. **92**, 201912 (2008).
[6] J. B. Philipp, P. Majewski, L. Alff, A. Erb, R. Gross, T. Graf, M. S. Brandt, J. Simon, T. Walther, W. Mader, D. Topwal, and D. D. Sarma, Phys. Rev. B **68**, 144431 (2003).
[7] D. D. Sarma, Curr. Opin. Solid State Mater. Sci. **5**, 261 (2001).
[8] B. Garcia Landa, C. Ritter, M. R. Ibarra, J. Blasco, P. A. Algarabel, R. Mahendiran, and J. García, Solid State Commun. **110**, 435 (1999).
[9] B. Martinez, J. Navarro, L. Balcells, and J. Fontcuberta, J. Phys.:

Condens. Matter **12**, 10515 (2000).
[10] D. D. Sarma, S. Ray, K. Tanaka, M. Kobayashi, A. Fujimori, P. Sanyal, H. R. Krishnamurthy, and C. Dasgupta, Phys. Rev. Lett. **98**, 157205 (2007).
[11] C. L. Yuan, S. G. Wang, W. H. Song, T. Yu, J. M. Dai, S. L. Ye, and Y. P. Sun, Appl. Phys. Lett. **75**, 3853 (1999).
[12] D. D. Sarma, E. V. Sampathkumaran, R. Sugata, R. Nagarajan, S. Majumdar, A. Kumar, G. Nalini, and T. N. Gururow, Solid State Commun. **114**, 465 (2000).
[13] Cz. Kapusta, P. C. Riedi, D. Zajac, M. Sikora, J. M. De Teresa, L. Morellon, and M. R. Ibarra, J. Magn. Magn. Mater. **242-245**, 701 (2002).
[14] K. Kuepper, M. Kadiroglu, A. V. Postnikov, K. C. Prince, M. Matteucci, V. R. Galakhov, H. Hesse, G. Borstel, and M. Neumann, J. Phys.: Condens. Matter **17**, 4309 (2005).
[15] Y. Tomioka, T. Okuda, Y. Okimoto, R. Kumai, K.-I. Kobayashi, and Y. Tokura, Phys. Rev. B **61**, 422 (2000).
[16] Dinesh Topwal, D. D. Sarma, H. Kato, Y. Tokura, and M. Avignon, Phys. Rev. B **73**, 094419 (2006).
[17] D. D. Sarma, P. Mahadevan, T. Saha-Dasgupta, S. Ray, and A. Kumar, Phys. Rev. Lett. **85**, 2549 (2000).
[18] Z. Szotek, W. M. Temmerman, A. Svane, L. Petit, and H. Winter, Phys. Rev. B **68**, 104411 (2003).
[19] V. Kanchana, G. Vaitheeswaran, M. Alouani, and A. Delin, Phys. Rev. B **75**, 220404(R) (2007).
[20] I. V. Solovyev, Phys. Rev. B **65**, 144446 (2002).
[21] A. Chattopadhyay and A. J. Millis, Phys. Rev. B **64**, 024424 (2001).
[22] O. Navarro, E. Carvajal, B. Aguilar, and M. Avignon, Physica B **384**, 110 (2006).
[23] J. Kanamori and K. Terakura, J. Phys. Soc. Jpn. **70**, 1433 (2001).
[24] E. Carvajal, O. Navarro, R. Allub, M. Avignon, and B. Alascio, Eur. Phys. J. B **48**, 179 (2005).
[25] L. Brey and M. J. Calderón, S. Das Sarma, and F. Guinea, Phys. Rev. B **74**, 094429 (2006).
[26] J. L. Alonso, L. A. Fernandez, F. Guinea, F. Lesmes, and V. Martin-Mayor, Phys. Rev. B **67**, 214423 (2003).
[27] P. Sanyal and P. Majumdar, Phys. Rev. B **80**, 054411 (2009).
[28] Z. Fang, K. Terakura, and J. Kanamori, Phys. Rev. B **63**, 180407(R) (2001).
[29] J. van den Brink, G. Khaliullin, and D. Khomskii, Phys. Rev. Lett. **83**, 5118 (1999).
[30] A. Kahoul, A. Azizi, S. Colis, D. Stoeffler, R. Moubah, G. Schmerber, C. Leuvrey, and A. Dinia, J. Appl. Phys. **104**, 123903 (2008).
[31] T. Saitoh, M. Nakatake, H. Nakajima, O. Morimoto, A. Kakizaki, Sh. Xu, Y. Moritomo, N. Hamada, and Y. Aiura, J. Electron Spectrosc. Relat. Phenom. **144-147**, 601 (2005).
[32] G. Kresse and J. Hafner, Phys. Rev. B **47**, 558 (1993); G. Kresse and J. Furthmuller, *ibid.* **54**, 11169 (1996).
[33] O. K. Andersen and T. Saha-Dasgupta, Phys. Rev. B **62**, R16219 (2000).
[34] J. P. Perdew, J. A. Chevary, S. H. Vosko, K. A. Jackson, M. R. Pederson, D. J. Singh, and C. Fiolhais, Phys. Rev. B **46**, 6671 (1992); **48**, 4978(E) (1993).
[35] V. I. Anisimov, F. Aryasetiawan, and A. I. Liechtenstein, J. Phys. Condens. Matter **9**, 767 (1997).
[36] P. E. Blöchl, Phys. Rev. B **50**, 17953 (1994); G. Kresse and D. Joubert, *ibid.* **59**, 1758 (1999).
[37] O. K. Andersen, Phys. Rev. B **12**, 3060 (1975).
[38] J. Navarro, C. Frontera, Ll. Balcells, B. Martínez, and J. Fontcuberta, Phys. Rev. B **64**, 092411 (2001).
[39] C. Frontera, D. Rubi, J. Navarro, J. L. Garcia-Munoz, J. Fontcuberta, and C. Ritter, Phys. Rev. B **68**, 012412 (2003).
[40] Carlos Frontera (private communication).
[41] Optimization has been carried out both in terms of GGA and GGA+U. The results are found to differ only marginally. The values quoted in Table I were obtained with GGA.
[42] J. Navarro, J. Fontcuberta, M. Izquierdo, J. Avila, and M. C. Asensio, Phys. Rev. B **70**, 054423 (2004).
[43] Z. Zhang and S. Satpathy, Phys. Rev. B **44**, 13319 (1991).
[44] T. Saha-Dasgupta, Molly De Raychaudhury, and D. D. Sarma, Phys. Rev. Lett. **96**, 087205 (2006).
[45] There are nine degrees of freedom per Fe-Mo pair, consisting of three at Fe site and six at Mo site.
[46] C. Meneghini, Sugata Ray, F. Liscio, F. Bardelli, S. Mobilio, and D. D. Sarma, Phys. Rev. Lett. **103**, 046403 (2009).
[47] S. Ray (private communication).
[48] H. Das, P. Sanyal, T. Saha-Dasgupta, and D. D. Sarma (unpublished).